From:	em.comstr.0.718173.672ac661@editorialmanager.com on behalf of Composite Structures <em@editorialmanager.com>
Sent:	22 February 2021 08:57
To:	Tobias Laux
Subject:	Decision on submission to Composite Structures

Manuscript Number: COMSTR-D-20-02043R1

Modelling damage in multidirectional laminates subjected to multi-axial loading: ply thickness effects and model assessment

Dear Mr Laux,

Thank you for submitting your manuscript to Composite Structures.

I am pleased to inform you that your manuscript has been accepted for publication.

My comments, and any reviewer comments, are below. Your accepted manuscript will now be transferred to our production department. We will create a proof which you will be asked to check, and you will also be asked to complete a number of online forms required for publication. If we need additional information from you during the production process, we will contact you directly.

We appreciate you submitting your manuscript to Composite Structures and hope you will consider us again for future submissions.

Kind regards,
Antonio Ferreira
Editor

Modelling damage in multidirectional laminates subjected to multi-axial loading: ply thickness effects and model assessment

Tobias Laux[a,b*], Khong Wui Gan[a,c], Rodrigo P. Tavares[d,e,f], Carolina Furtado[d,e,g], Albertino Arteiro[d,e], Pedro P. Camanho[d,e], Ole T. Thomsen[b], Janice M. Dulieu-Barton[a,b]

[a] School of Engineering, University of Southampton, Highfield, SO17 1BJ, Southampton, UK

[b] University of Bristol, Bristol Composites Institute, School of Civil, Aerospace and Mechanical Engineering, Queen's Building, University Walk, Bristol, BS8 ITR, UK

[c] School of Engineering, University of Southampton Malaysia, Kota Ilmu Educity @ Iskandar, 79200 Iskandar Puteri, Johor, Malaysia

[d] DEMec, Faculdade de Engenharia, Universidade do Porto, Rua Dr. Roberto Frias, s/n, 4200-465 Porto, Portugal

[e] INEGI, Instituto de Ciência e Inovação em Engenharia Mecânica e Engenharia Industrial, Rua Dr. Roberto Frias, 400, 4200-465 Porto, Portugal

[f] Mechanics of Materials and Structures (UGent-MMS), Department of Materials, Textiles and Chemical Engineering, Ghent University, Technologiepark-Zwijnaarde 46, 9052, Zwijnaarde, Belgium

[g] Department of Aeronautics and Astronautics, Massachusetts Institute of Technology, 77 Massachusetts Avenue, Cambridge, MA 02139, United States

*tslx@msn.com

Abstract

A meso-scale damage modelling framework for composite laminates is assessed against multi-axial experimental data obtained from specimens subjected to combined tension/compression and shear loading using a modified Arcan fixture (MAF). Two laminates made from unidirectional carbon fibre-reinforced epoxy plies of different thickness are considered to investigate the ply thickness effect on the damage behaviour of modified open-hole specimens. Intra-laminar damage is predicted using a continuum damage model combined with a fibre-aligned mesh, while cohesive zones are used to account for inter-laminar damage. The multi-axial open-hole specimen strength is predicted with a mean relative error of 15% across all the

investigated lay-up and loading configurations, while the predicted damage maps show encouraging agreement with full-field measurements obtained using digital image correlation (DIC). However, the assessment reveals limitations of the assumption of small strains and rotations in the formulation of the model that leads to spurious model behaviour for shear-dominated damage modes.

1   Introduction

Multidirectional composite laminates made from unidirectional (UD) fibre-reinforced polymers (FRP) are widely used in the design of lightweight structures. Their failure modes and strengths depend not only on the properties of the constituent materials, but also on the laminate lay-up (*i.e.* the fibre orientations, the ply thickness and the stacking sequence), and on the stress state in the material [1,2]. Efficient design and validation of FRP structures requires tools that can accurately predict the progressive failure from damage initiation and evolution to ultimate failure of a wide range of composite materials and laminate lay-ups subjected to general multi-axial loading conditions. The integration of such 'virtual testing' techniques into design, validation and ultimately certification of composite structures has the potential to reduce cost and time-to-market and to accelerate the development of new materials and structural concepts [3,4].

To simulate progressive failure in multidirectional composite laminates several meso-scale modelling frameworks based on the finite element method (FEM) have been proposed [4,5,14–17,6–13] where the homogenised UD ply is the basic building block. The failure mode concept-based approach adopted by these meso-scale models considers the progressive failure of the fibres, matrix, and interfaces separately. The models presented in [4,6–9] are based on continuum-damage models (CDMs) for all intra-laminar failure mechanisms (fibre tensile failure, fibre kinking, matrix cracking), whereas inter-laminar failure (delamination) is accounted for discretely using cohesive zone models [5]. The use of a CDM framework implies

that intra-laminar cracks are not accounted for discretely between the different phases of fibre and matrix but instead are "smeared" (homogenised) over the finite elements. This means the modelled crack growth may become dependent on the mesh size, which can be avoided by introducing a characteristic element length [18,19] and by using fibre aligned meshes to mitigate some of the mesh induced directional bias [7]. Other meso-scale models overcome the difficulties associated with CDMs by modelling intra-laminar matrix cracking discretely using cohesive zones [11–14] or by means of the eXtended FEM (X-FEM) approach or its variations [15–17]. Regardless of the selected modelling framework, it is particularly useful for virtual testing to discretise the laminate at the meso-scale level (*i.e.* ply-by-ply discretisation), as laminate lay-up effects can be accounted for, and most of the basic ply properties can be obtained with relatively simple mechanical tests [4].

While the application of meso-scale models to large structures is currently limited by their high computational cost, they can be used to simulate failure in multidirectional coupon specimens or small sub-components to gain a detailed understanding of failure modes and their interactions. Common experiments used to validate progressive damage models are the open-hole tension (OHT) and compression (OHC) tests. They are suitably complex to assess the predictive capability of progressive failure models, as the failure behaviour is not only dependent on the UD material system but also on the laminate lay-up, the overall specimen geometry, and the size of the hole [20].

From the above survey of the open literature [4,6,7,10,14,17,20,21], it can be concluded that OHT and OHC ultimate strength predictions currently lie within a mean relative error of roughly 10% compared to experimental results, and that the progressive nature of failure is in good agreement for a range of laminate lay-ups and specimen geometries. However, these modelling frameworks have not been rigorously assessed with regard to their ability to accurately simulate failure for more complex multi-axial loading conditions in which the interaction of failure mechanisms is different. Therefore, multi-axial experiments have been proposed for model validation. Cruciform specimens loaded in tension-tension, compression-

compression, or tension-compression have been proposed in [22], while Tan *et al.* [1,9] assessed model predictions against open-hole experimental data obtained for the combined tension-shear, but not the compression-shear loading regime.

In [23], multi-axial open-hole tests were conducted using a new modified Arcan fixture (MAF), based on the MAF in [24,25], not only in the combined tension-shear, but also in the compression-shear loading regime. Three quasi-isotropic carbon/epoxy laminates with different lay-ups were studied, using the full-field technique of digital image correlation (DIC), from which a significant influence of the ply thickness on the multi-axial open-hole specimen strength was observed. Thus, in the present paper, a state-of-the-art meso-scale model is used to simulate progressive failure in quasi-isotropic carbon/epoxy laminates with two different UD ply thicknesses subjected to combined tension/compression and shear loading. It is the aim, for the first time, to assess and validate the capability of the model to predict the experimentally observed interdependence of ply thickness and multi-axial loading effects in [23]. The meso-scale model is based on the CDM presented in [4] for the UD plies, and the cohesive zone model developed in [26,27] for the interfaces. Intra-laminar failure is predicted using a modified version of the LaRC03/04 criterion [28,29]. It should be noted that a large variety of alternative approaches to model damage exist [30–32], of which the LaRC criterion is one of the most promising. A FEM modelling strategy is proposed based on structured, fibre-aligned meshes that is able to account for the interaction between inter- and intra-laminar damage for all of the investigated combined load cases. The strength of the used modelling framework is its potential to predict damage initiation and evolution under general (multiaxial) loading conditions over a wide range of laminate architectures with different ply thicknesses and fibre orientation angles [4]. Hence its use enables the model predictions to be used in combination with the experimental data to further investigate the effect of ply thickness on the progressive failure behaviour.

To the knowledge of the authors, the capability of a meso-scale model to predict failure of multidirectional open-hole specimens in the full tension/compression and shear loading regime

has yet to be investigated. Thus, the purpose of the research presented is to advance the maturity and ultimately the industry-readiness of predictive computational modelling tools for composite laminates developed for 'virtual testing', and to inform the further direction of model development through a rigorous validation against full-field, multi-axial, high-fidelity experimental data.

2 Combined tension/compression and shear testing

In [23], a multi-axial testing campaign was described on open-hole specimens, of the geometry shown in Figure 1 (a), which forms the basis for the simulations described in the present paper. The specimens were manufactured using an out-of-autoclave UD carbon/epoxy prepreg system with the lay-ups given in Table 1. The laminates were consolidated at a pressure of 1 bar and at an elevated temperature of 90° C. Laminate 1 consists of 8 'thick' plies, whereas Laminate 2 consists of 16 'thin' plies, which are approximately half the thickness (t_{ply}) of the 'thick' ones. Note that the surface plies of Laminate 2 have approximately half the thickness of the embedded plies, which is accounted for in the FEM model. The fibres in both laminates are oriented at the standard quasi-isotropic fibre orientation angles $\theta = 0°$, $+/-45°$, and $90°$, defined relative to

the y-axis of the specimen as shown in Figure 1 (a). The overall thickness of both laminates (t_{lam}) and their homogenised laminate elastic properties are similar according to classical lamination theory (CLT) [33]. Differences in their failure behaviour can therefore be attributed to the UD ply thickness effect. The specimens were subjected to combined tension/compression and shear loading using the MAF shown in Figure 1 (b). In the test, the choice of the loading hole pair used to connect the MAF to the universal test machine as designated by the loading angle α, defined the combined tension/compression and shear load cases, as shown in Figure 1 (b). In [23], the specimens were loaded in tension ($\alpha = 0°$), combined tension-shear ($\alpha = 15°$, $45°$), shear ($\alpha = 90°$), combined compression-shear ($\alpha = 135°$, $165°$) and compression ($\alpha = 180°$). If P is the applied load, then the load-based failure envelope is defined by the normal

component of the load, $N_y = P\cos(\alpha)$, and the shear component of the load, $N_{yx} = P\sin(\alpha)$, as shown in Figure 1 (a). P is transferred to the specimen through knurled friction grips of the MAF. The experimental study presented in [23] provided the full-field displacement and strain maps obtained using stereo DIC on one side of the specimen, an example of which is shown in Figure 1 (b). These surface measurements are used in the present study to validate the model predictions. (Full details of the experimental development of the MAF procedure and application of DIC are given in [23,34].)

3 Meso-scale finite element model

3.1 Finite element modelling strategy

The commercial FEM software ABAQUS/Explicit 6.14-3 [35] is used to simulate the MAF experiments. The physical boundary conditions imposed by the MAF on the specimens, as shown in Figure 1 (b), are simplified in the modelling space as shown in Figure 2, ignoring the clamped area of the specimen. The boomerang shaped arms of the MAF are modelled by multi point constraints (MPC) of type 'beam', while the loading holes in the MAF arms are represented by reference nodes in the model space (see Figure 2 (a)). The position of the reference nodes is determined by the loading angle α and defines, like the choice of the loading hole pair in the experiment (see Figure 1(b)), the combined tension/compression-shear load case applied. The bottom reference node is fixed, whereas a velocity boundary condition is imposed on the top reference node up to ultimate failure. The proposed modelling set-up accounts for the effect of the kinematics imposed on the specimen by the MAF rig 'mechanism' (see Figure 1). However, the boundary conditions ignore the compliance of the MAF rig and of the knurled friction interfaces between the grips and the specimen. It is assumed in the FEM model that the top and bottom edge of the specimen is fully fixed relative to the arms, which is not strictly fulfilled as the clamping mechanism allows for some compliance between the grips and the specimen.

To reduce the computational cost, the through-thickness symmetry of the lay-ups is exploited by applying symmetry boundary conditions on the mid-plane of the specimen as shown in Figure 2 (b). The multidirectional laminates are modelled on the meso-scale with the homogenised UD plies as the basic building blocks as shown in Figure 3. Intra-laminar damage (fibre failure and in-plane matrix cracking) is simulated using a user-defined material model (VUMAT) based on the CDM framework proposed by Furtado *et al.* [4], which is described in more detail in Section 3.2. Inter-laminar failure between the plies (delamination) is accounted for using cohesive surfaces placed between the plies as shown in Figure 3 (b), which are described in Section 3.3. A structured fibre-aligned mesh, as shown in Figure 3 (a), was used to mitigate some of the mesh induced directional bias of the CDM on the prediction of intra-laminar crack propagation [7,8,22]. This enabled a physically more accurate prediction of subcritical inter- and intra-laminar matrix cracks and their interactions, which is crucial in the prediction of the multi-axial open-hole specimen strength of the laminates. The plies are meshed with a single layer of linear reduced integration solid elements through the ply thickness. The mesh consists predominantly of $0.35 \times 0.35 \times t_{ply}$ mm³ brick elements (C3D8R) with some wedge elements (C3D6) along the curved edges and around the hole (see Figure 3 (a)). The element size is informed by previous analyses conducted in [4], where the failure behaviour of OHT and OHC test specimens were simulated. The mesh was designed using the commercial CAD software Rhino 5 [36] and was then imported into the FEM software ABAQUS/Explicit [35].

A quasi-static explicit dynamic analysis was conducted to avoid convergence issues due to nonlinear material behaviour, including strain softening, discrete cohesive failure and contact. To reduce computational cost, the loaded reference node was displaced at an increased loading rate of 100 mm/s. The velocity boundary condition was applied via a smooth step loading amplitude for 1/10 of the total simulated displacement. To further accelerate the analysis, variable semi-automatic mass scaling was imposed on elements with a stable time increment smaller than 1×10^{-7} s. To meet the typical requirements for a quasi-static analysis, it was

ensured that the kinetic energy was below 5% of the internal strain energy throughout the analysis [35].

3.2 The ply continuum damage model (CDM)

Consider a UD fibre-reinforced composite ply with the x_1 axis parallel to the fibres, the x_2 axis transverse to the fibres and the x_3 axis perpendicular to the plane of the ply. Assuming that the UD ply is transversely isotropic with respect to the fibre direction ($E_3 = E_2$, $G_{13} = G_{12}$, $v_{13} = v_{12}$ $G_{23} = E_2 / (2(1 + v_{23}))$), the 3D lamina stress-strain relationship is described by:

$$
\begin{bmatrix} \epsilon_{11} \\ \epsilon_{22} \\ \epsilon_{33} \\ \gamma_{12} \\ \gamma_{13} \\ \gamma_{23} \end{bmatrix} = \begin{bmatrix} H_{11} & H_{12} & H_{13} & 0 & 0 & 0 \\ H_{12} & H_{22} & H_{23} & 0 & 0 & 0 \\ H_{13} & H_{23} & H_{33} & 0 & 0 & 0 \\ 0 & 0 & 0 & H_{44} & 0 & 0 \\ 0 & 0 & 0 & 0 & H_{55} & 0 \\ 0 & 0 & 0 & 0 & 0 & H_{66} \end{bmatrix} \begin{bmatrix} \sigma_{11} \\ \sigma_{22} \\ \sigma_{33} \\ \tau_{12} \\ \tau_{13} \\ \tau_{23} \end{bmatrix}
\tag{1}
$$

where ϵ_{ii} and γ_{ij} are the normal and shear strain components, σ_{ii} and τ_{ij} are the normal and shear stress components with $i, j = 1, 2, 3$, and where **H** is the compliance matrix with its components defined as [37]:

$$
H_{11} = \frac{1}{(1-d_1)|\sigma_{11}|}\left(\frac{\langle \sigma_{11} \rangle}{E_1} + \frac{\langle -\sigma_{11} \rangle}{E_{1c}} \right); \quad H_{22} = \frac{1}{(1-d_2)E_2}; \quad H_{33} = \frac{1}{(1-d_3)E_2}
$$

$$
H_{44} = \frac{1}{(1-d_6)G_{12}}; \quad H_{55} = \frac{1}{(1-d_5)G_{12}}; \quad H_{66} = \frac{1}{(1-d_4)G_{23}}
\tag{2}
$$

$$
H_{12} = -\frac{v_{12}}{|\sigma_{11}|}\left(\frac{\langle \sigma_{11} \rangle}{E_1} + \frac{\langle -\sigma_{11} \rangle}{E_{1c}} \right); \quad H_{13} = -\frac{v_{12}}{|\sigma_{11}|}\left(\frac{\langle \sigma_{11} \rangle}{E_1} + \frac{\langle -\sigma_{11} \rangle}{E_{1c}} \right); \quad H_{23} = -\frac{v_{23}}{E_2}
$$

where d_1, d_2 and d_6 are the scalar damage variables associated with fibre, matrix and shear damage, respectively. Furthermore, E_1 and E_{1c} are the fibre longitudinal tensile and compressive Young's moduli to account for any variations in longitudinal tension and compression, G_{12} and G_{23} are the in-plane and out-of-plane shear moduli, while v_{12} and v_{23} are the in-plane and out-of-plane Poisson's ratios, respectively. The Macaulay bracket $\langle \bullet \rangle$ in

8

Equation (2) returns the argument $\bullet$ if positive or zero otherwise. The elastic properties of the UD ply used to inform the model and the associated test methods used for their determination are reported in Table 2.

To account for the effect of crack closure under load reversal on d_1 and d_2, it is necessary to track damage caused by tension (d_{1+}, d_{2+}) separately from damage caused by compression (d_{1-}, d_{2-}) as:

$$d_1 = d_{1+} \frac{\langle \sigma_{11} \rangle}{|\sigma_{11}|} + d_{1-} \frac{\langle -\sigma_{11} \rangle}{|\sigma_{11}|} \qquad (3)$$

$$d_2 = d_{2+} \frac{\langle \sigma_{22} \rangle}{|\sigma_{22}|} + d_{2-} \frac{\langle -\sigma_{22} \rangle}{|\sigma_{22}|} \qquad (4)$$

where the sign of the corresponding normal stress defines if a damage mode is either passive or active. For shear damage only one damage variable (d_6) is defined, since shear cracks cannot close under load reversal.

The domain of the elastic response (no damage) of the UD ply under a complex stress state is defined by an approximation of the LaRC03-04 failure criteria [28,29]. Four separate damage activation functions are defined for longitudinal fibre tensile failure (ϕ_{1+}), longitudinal fibre compressive failure (ϕ_{1-}), transverse matrix failure where the fracture plane is perpendicular (ϕ_{2+}), or not perpendicular to the mid-plane of the ply (ϕ_{2-}). Thereby, fibre tensile failure is predicted using the simple maximum stress criterion defined as:

$$\phi_{1+} = \frac{E_1}{X_T} \epsilon_{11} \qquad (5)$$

where X_T is the longitudinal fibre tensile strength. For transverse matrix failure where the fracture plane is perpendicular to the mid-plane of the ply, two failure functions are defined for transverse tensile and moderate transverse compressive stress states defined as:

$$\phi_{2+} = \begin{cases} \sqrt{\left(1-\dfrac{\mathscr{G}_{2+}}{\mathscr{G}_6}\right)\dfrac{\sigma_{22}}{Y_T} + \left(\dfrac{\mathscr{G}_{2+}}{\mathscr{G}_6}\right)\left(\dfrac{\sigma_{22}}{Y_T}\right)^2 + \left(\dfrac{\tau_{12}}{Y_T}\right)^2} & \text{if } \sigma_{22} \geq 0 \\[2mm] \dfrac{1}{S_L}\left\langle |\tau_{12}| + \eta^L \sigma_{22}\right\rangle & \text{if } \sigma_{22} < 0 \end{cases} \tag{6}$$

where Y_T is the transverse tensile strength, S_L is the shear strength and $\mathscr{G}_{2+}$, $\mathscr{G}_6$ are the energies associated with transverse tensile and shear fracture. For transverse tension, the failure criterion is quadratic with respect to the transverse and shear stresses. For transverse compressive stresses the criterion is based on the Mohr-Coulomb hypothesis and accounts for the shear strength enhancement when transverse compression is applied, where

$$\eta^L \approx -\frac{S_L \cos(2\alpha_0)}{Y_C \cos^2 \alpha_0} \tag{7}$$

is the longitudinal friction coefficient. Fibre compression failure is predicted using a fibre kinking model defined by:

$$\phi_{1-} = \frac{1}{S_L^*}\left\langle |\tau_{12}^R| + \eta_L \sigma_{22}^R \right\rangle \tag{8}$$

where failure occurs when the stresses in the coordinate system associated with the rotated (or kinked) fibres, σ_{22}^R and τ_{12}^R, reach the limit stress state for matrix cracking defined in Equation (6). S_L^* in Equation (8) is an effective shear strength calculated by imposing that, at failure, the 2D damage activation function (given in Equation (8)) is equal to the 3D damage activation function proposed in [38]. This modification to LaRC03/04 [28,29] is described in detail in [4] and improves the model's ability to account for the effect of though-thickness stresses on fibre kinking failure. The stresses in the rotated coordinate system are given by:

$$\sigma_{22}^R = \sigma_{11}\sin^2\varphi^C + \sigma_{22}\cos^2\varphi^C - 2|\tau_{12}|\sin\varphi^C\cos\varphi^2 \tag{9}$$

$$\tau_{22}^R = (\sigma_{22} - \sigma_{11})\sin\varphi^C\cos\varphi^C + |\tau_{12}|(\cos^2\varphi^C - \sin^2\varphi^C) \tag{10}$$

where φ^C is the critical fibre misalignment angle of a UD ply subjected to uniaxial compression at failure stress, X_C, defined as:

10

$$\varphi^C = \arctan\left(\frac{1 - \sqrt{1 - 4(S_L / X_C + \eta^L)S_L / X_C}}{2(S_L / X_C + \eta^L)}\right) \tag{11}$$

Transverse matrix failure for the case of high transverse compression load is also modelled based on the Mohr-Coulomb hypothesis. It is assumed that failure results from a quadratic interaction between the effective shear stresses acting on the fracture plane (τ_L^{eff} and τ_T^{eff}):

$$\phi_{2-} = \sqrt{\left(\frac{\tau_{eff}^T}{S_T}\right)^2 + \left(\frac{\tau_{eff}^L}{S_L}\right)^2} \quad \text{if } \sigma_{22} < 0 \tag{12}$$

where τ_L^{eff} and τ_T^{eff} are given by:

$$\tau_{eff}^T = \left\langle -\sigma_{22}\cos\alpha_0(\sin\alpha_0 - \eta^T\cos\alpha_0\cos\theta)\right\rangle \tag{13}$$

$$\tau_{eff}^L = \left\langle \cos\alpha_0(|\tau_{12}| + \eta^L\sigma_{22}\cos\alpha_0\sin\theta)\right\rangle \tag{14}$$

and where the transverse shear strength can be approximated by:

$$S_T = Y_C\cos(2\alpha_0) + \frac{\cos\alpha_0}{\tan\alpha_0} \tag{15}$$

α_0 in Equations (13) to (15) is the angle of the fracture plane in respect to the through-thickness x_3 axis in a UD ply subjected to uniaxial transverse compression at failure stress, Y_C, assumed to be approximately 53° [28,29]. Moreover, η^T, is the transverse friction coefficient approximated by:

$$\eta^T \approx \frac{-1}{\tan(2\alpha_0)} \tag{16}$$

and θ is the sliding angle defined as the angle between the resultant shear traction vector on the fracture plane and the transverse direction (x_2-axis) given by:

$$\theta = \arctan(\frac{-|\sigma_{12}|}{\sigma_{22}\sin\alpha_0}) \tag{17}$$

Based on the failure functions given in Equations (5), (6), (8) and (12), the elastic domain thresholds, r_i ($i = 1+, 1-, 2+, 2-$), accounting for load reversals, are defined as:

$$r_{1+} = \max\{1, \max_{s=0,t}\{\phi_{1+}^s\}, \max_{s=0,t}\{\phi_{1-}^s\}\} \tag{18}$$

11

$$r_{1-} = \max\{1, \max_{s=0,t}\{\phi_{1-}^s\}\} \tag{19}$$

$$r_{2+} = \max\{1, \max_{s=0,t}\{\phi_{2+}^s\}, \max_{s=0,t}\{\phi_{2-}^s\}\} \tag{20}$$

$$r_{2-} = \max\{1, \max_{s=0,t}\{\phi_{2-}^s\}\} \tag{21}$$

The distinction between r_{1+} and r_{1-} is introduced to account for the assumption that cracks

caused by longitudinal tensile loading (ϕ_{1+}) close under load reversal, leaving the elastic domain

unchanged, while kink bands formed under fibre compressive stresses (ϕ_{1-}) further inflict

damage upon load reversal and thus increase the elastic domain. Similarly, transverse cracks

that are perpendicular to mid-plane of the ply (ϕ_{2+}) close when compressive load is applied and

therefore leave the elastic domain unchanged while cracks which are not perpendicular to the

ply mid-plane (ϕ_{2-}) inflict further damage upon load reversal and thus increase the elastic

domain. r_i take the value of 1 when the material is undamaged and increase with the evolution

of damage. They are linked back to the damage variables in Equation (2) via the damage

evolution laws governed by the fracture toughness ($\mathcal{G}_{1+}$, $\mathcal{G}_{1-}$, $\mathcal{G}_{2+}$, $\mathcal{G}_{2-}$, $\mathcal{G}_6$) associated with each

damage mode and the assumed softening laws as shown in Figure 4. In longitudinal tension

(Figure 4 (a)) the initially linear elastic response is followed by a bi-linear softening law after

longitudinal tensile damage is identified. In longitudinal compression (Figure 4 (b)), the initially

linear elastic ply behaviour is followed by a bi-linear softening law where the first segment is

associated with the formation of kink bands while the second horizontal segment is associated

with kink band broadening under constant stress. The initially linear elastic stress-strain

behaviour in transverse tension and compression (Figure 4 (c)) is followed by a simple linear

softening law. Finally, the nonlinear behaviour of UD composites in shear is accounted for by

assuming a bi-linear shear stress-strain relationship as shown in Figure 4 (d), where S_L^P defines

the onset of shear nonlinearity, and where K_P is the shear incremental stiffness under 'plastic'

flow. After failure in shear, the elastic properties are degraded following a linear softening law

(Figure 4 (d)). The shapes of the softening laws are described based on the fracture toughness of

each failure mechanism, the shape parameters (f_{XC}, f_{XT}, f_{GT} – see Figure 4) and the characteristic length l^* of the finite element [18]. l^* is introduced to ensure correct energy dissipation during damage growth and to avoid mesh size dependency of the numerical solution. The strengths of the UD ply and the methods used for their determination are reported in Table 3.

Apart from the uniaxial strengths, the model requires the input of the biaxial tensile (Y_{BT}) and compressive (Y_{BC}) strengths. These values were scaled based on the uniaxial strengths according to [4] and are reported in Table 3. The parameters for the non-linear shear stress-strain relationship (S_L^P, K_P) were determined by a judiciously selected bi-linear fit to the shear stress-strain curves obtained using butterfly specimens using the MAF in [24], [34].

The fracture toughness values and the parameters governing the shapes of the softening laws in Figure 4 are given in Table 4. Due to the lack of experimental data, they were selected based on a sensitivity study, where the bounds on the toughness values were determined from values reported in the literature for the well-characterised IM7/8552 and T800/M21 carbon/epoxy material systems [4]. Investigating four different fracture toughness combinations, the average coefficient of variation in the predicted multi-axial open-hole specimen strengths for Laminate 1 across all load cases was 3%. Considering the relatively low sensitivity of the ultimate strength to the selection of fracture toughness, the best fit was used in the simulations as provided in Table 4. Furthermore, the transverse and shear strengths of a UD ply embedded in a multidirectional laminate depend on the ply thickness (t_{ply}) and on the position of the ply in the laminate stack (embedded vs. surface ply) [39–42]. Therefore, the in-situ strengths (Y_T^{is}, S_L^{is}, Y_C^{is}) are calculated for both Laminates 1 and 2 based on the fracture mechanics models presented in [4], which account for the bi-linear shear stress-strain curves assumed in the model. The derived in-situ strengths are reported in Table 5. It is observed that the in-situ strengths for the 'thin' ply Laminate 2 are either equal or higher than the ones for the 'thick' ply Laminate 1. For further details of the CDM framework used in this work, the reader is referred to [4,37].

More details on the testing program conducted to obtain the material properties used to inform the ply damage model are given in [34].

3.3 Cohesive zone model

Inter-laminar failure (delamination) is modelled using the mixed-mode cohesive zone models proposed by Camanho *et al.* [26] and Turon *et al.* [27] as implemented into the surface contact algorithms native to ABAQUS/Explicit [35]. Failure is identified by means of a quadratic failure criterion based on the inter-laminar normal (τ_n) and shear (τ_{sh}) strengths. Damage growth is governed by the Benzeggagh-Kenane (BK) mixed-mode damage propagation criterion. The linear traction-separation laws are informed by the interlaminar mode I and II critical fracture energies G_{IC} and G_{IIC} respectively, and the mixed mode interaction parameter, η_{B-K}. The material input parameters informing the cohesive zone model are given in Table 6: The initial penalty stiffness (K_n) is selected according to recommendations in [26], τ_n is set equal to Y_T, whereas τ_{sh} was measured using the ILSS test [43]. The remaining interface properties were taken from the IM7/8552 carbon/epoxy material system [4].

4 Simulation results and model validation

4.1 Linear elastic load response

Before assessing the predictive capability of the progressive meso-scale damage model, predicted surface strain maps are validated against surface strains obtained experimentally using DIC in specimens loaded within the linear/elastic load response. This allows the validation of the simplified boundary conditions adopted in the FEM (see Figure 2), and the elastic material properties used to inform the model (see Table 2). Therefore, DIC strain maps for a Laminate 1 specimen loaded in tension ($\alpha = 0°$) and shear ($\alpha = 90°$) are shown in Figure 5 and 6, respectively. The two cases are shown as examples, because the strain fields for all other load

cases within the linear elastic loading regimes are simple linear superpositions of the compared fields of Figure 5 and 6.

It can be seen in the strain maps of the uniaxial tensile load case ($\alpha = 0°$) in Figure 5 that the dominant vertical strains (ϵ_{yy}) predicted by FEM are in good agreement with the experimental results. This includes the significant strain concentrations to both sides of the hole. As expected, the x-direction normal (ϵ_{xx}) and shear strains (γ_{xy}) are low for this load case, and therefore the signal-to-noise ratio in the DIC maps is relatively poor, obscuring some of the strain features. Nevertheless, the ϵ_{xx} strain concentrations at the top right and bottom left edges, as well as the γ_{xy} strain concentrations at the hole edge, show reasonable agreement between FEM predictions and DIC strain maps. The apparent over-prediction of the ϵ_{xx} normal strain concentrations at the top and bottom edge of the hole is attributed to a combination of the low signal-to-noise ratio in the DIC maps, the assumption of linear elasticity in the model (ignoring the strain redistribution mechanisms due to material nonlinearity), and to the assumption of rigid x-direction boundary conditions at the top and bottom edges of the model (see Section 3.1). It is assessed that the rigid x-direction boundary conditions cause an over prediction of the x-direction strains by the FEM. The predicted FEM strain maps are also in good agreement with the captured DIC strain maps for the shear load case ($\alpha = 90°$), as shown in Figure 6. The overall FEM strain patterns, as well as the magnitudes of the strain concentrations at the hole edge, match well with the experimental results.

The overall agreement between the predicted (FEM) and experimental (DIC) strain fields confirms that the elastic properties determined for the UD plies (see Table 2) are sufficiently accurate, that the assumed model boundary conditions (see Figure 2) are reasonable, and that the model set-up allows for a meaningful assessment and evaluation of the meso-scale damage model predictions against the experimental results see Sections 4.2 and 4.3).

4.2 Multi-axial open-hole specimen strength

The predicted multi-axial open-hole specimen failure envelopes for 'thick' ply Laminate 1 and 'thin' ply Laminate 2 are compared against the experimental data taken from [23] in the N_y - N_{yx} loading space in Figure 7 (a), while the initial derived predictive errors are shown in Figure 7 (b).

It is observed from the experimental data in Figure 7 (a) that ply thickness has a significant effect on the multi-axial open-hole specimen strength. The 'thin' ply laminate specimens are up to 147% stronger than 'thick' ply laminate specimens in combined tension-shear ($\alpha = 15°, 45°$), while the difference is relatively small in the uniaxial tension ($\alpha = 0°$), and in the combined compression-shear loading regimes ($\alpha = 90°$-$180°$). The size and shape of the simulated failure envelopes are in reasonable agreement with the experimental results: the 'thin' ply Laminate 2 specimens are predicted to be stronger than those made from the 'thick' ply Laminate 1 for all load cases apart from compression ($\alpha = 180°$), while the largest differences in specimen strength are also predicted in the combined tension-shear load regime ($\alpha = 0°$-$90°$). This demonstrates the ability of the FEM model to qualitatively predict ply-thickness effects on the multi-axial open-hole specimen strength.

However, it is observed from Figure 7 (b) that the predictive capability of the model varies significantly between the different load cases. The largest errors are associated with the tensile dominated load cases ($\alpha = 0°, 15°$) with a maximum error of 47%. For all other load cases the error is within +/− 27 %, while the best prediction is achieved for Laminate 1 in combined tension-shear ($\alpha = 45°$) with an error of −1%.

For the tensile-dominated load cases ($\alpha = 0°$ for Laminate 1 and $\alpha = 0°, 15°$ for Laminate 2), the discrepancies between the model predictions and the experimental data are significantly larger than would be expected from typical OHT test results [4]. Investigating the model predictions for the tensile-dominated load cases (under prediction of the specimen strength), has shown that the critical spurious failure event at ultimate load in the FEM model is linked to a sudden mesh

instability in regions subjected to high fibre tensile and shear stresses. This indicates that the typical fibre splitting damage in the 0° ply at the hole observed in the experiment is not captured accurately by the damage model. An example of this mesh instability is shown in Figure 8 (a) where the central 0° ply near the hole edge in a Laminate 1 specimen subjected to uniaxial tension ($\alpha = 0°$) is shown. A distinct 'zig-zag' pattern near the stress/strain concentration at the hole edge can be observed, which is related to the premature failure prediction. It was found that the mesh 'zig-zag' is associated with the prediction of intra-laminar shear damage, which is described by the shear damage variable d_6, as visualised in Figure 8. This was confirmed by limiting the maximum allowable shear damage (d_6^{max}) in the 0° ply to 0.8 (initially set to 1.0 – total stiffness degradation at the material point), which led to an increase of the predicted ultimate failure load by 25%, and also to a change in the predicted failure pattern. By limiting d_6^{max}, larger shear stresses/strains can be sustained by delaying spurious shear failure until the occurrence of fibre tensile failure. In the case where $d_6^{max} = 0.8$ (see Figure 8 (b)), longitudinal fibre splits develop at the hole edge which are not predicted for the cases where $d_6^{max} > 0.8$ (see Figure 8 (a)). The longitudinal fibre splits are directly responsible for the notch blunting effect, which leads to the increased strength by redistributing the stresses at the hole [44,45]. Note that $d_6^{max} = 0.8$ is selected, because it is the largest value (least intrusive model modification) for which a distinct change in the failure mode (occurrence of longitudinal fibre splits) is observed. Limiting d_6^{max} in Laminate 2, in the 0° plies for the uniaxial tension load case ($\alpha = 0°$), and in the 0° and +45° plies for the combined tension-shear load case ($\alpha = 15°$) also significantly improves the prediction of the ultimate failure load, as shown in Figure 9.

The difficulties for the CDM framework to predict the notch blunting effect is a result of the assumption of small strains and rotations in the formulation of the model. Therefore, a means of accounting for large shear deformations, *i.e.* accounting for large rotations, is likely to remedy this limitation [46,47]. For the investigated out-of-autoclave material system, accounting for large deformations would be especially important, because the material is more

compliant (see Table 2) and at the same time stronger (see Table 3) in the fibre direction than, for example, the autoclave-consolidated aerospace grade IM7/8552 carbon/epoxy material system [4], for which the CDM framework was originally developed. For this reason, the deformation in the 0° ply before catastrophic tensile fibre failure is expected to be higher in the out-of-autoclave material system, and accounting for large shear deformation in the model formulations is necessary to avoid the 'zig-zag' instability of the mesh. Furthermore, the use of fibre-aligned FEM meshes has been found to promote the 'zig-zag' instability, whereas it is suppressed to some extent in unstructured meshes. It is expected that the unstructured mesh imposes an inherent damage arresting mechanism that prohibits the spread of the sudden mesh instability, which for this specific load case has a positive effect on the predicted damage pattern. However, the unstructured mesh also arrests cracks that are physical, leading to spurious predictions of crack propagation [7]. For the cases where the mesh instability occurs, limiting the allowable shear damage variable $d_6^{\max}$ to 0.8 is therefore proposed as an 'engineering approach' to obtain a more accurate strength prediction for the material investigated, as well as the prediction of a physically more meaningful ultimate failure mode by postponing/supressing the spurious shear driven 'zig-zag' instability. The disadvantage of the proposed solution is that the model requires user-intervened input informed by validation from experimental results, and that it is load-case specific.

The final relative errors (E), calculated as $E = (x_{\mathrm{EXP}} - x_{\mathrm{FE}})/(1/2(x_{\mathrm{EXP}} + x_{\mathrm{FE}}))$ for the predicted multi-axial open-hole specimen strengths are reported in Table 7. Across all of the investigated load cases and laminate configurations, the modification to the maximum allowable shear damage variable resulted in a mean relative error of 15% in the predicted multi-axial open-hole specimen strength, while the maximum errors were 25% (conservative) for Laminate 1 loaded in tension, and 27% (non-conservative) for Laminate 2 loaded in shear. Considering that similar, or conceptually more advanced models [4,6,7,10,14,17,20,21], predict uniaxial (as opposed to multi-axial as addressed in this paper) OHT and OHC strengths within 10%, these

results are encouraging, particularly since more complex combined load cases were studied and a new material system was used for which some of the model input parameters were taken from similar, well-characterised material systems.

4.3 Damage visualisation

To visualise the predicted damage behaviour, ply-by-ply damage maps are plotted at the experimental failure initiation load, at the maximum failure load (P_{ult}), and post-ultimate failure (post-P_{ult}). The predicted ply-by-ply damage maps are then compared/validated against the experimental results described in [23]. At failure initiation and ultimate load, the predicted failure patterns are compared against stereo DIC measurements, while the final failure patterns are compared against photographs of the failed specimens. An example of this comparative analysis is shown for Laminate 1 for combined tension-shear loading ($\alpha = 45°$) in Table 8, and for combined compression-shear loading ($\alpha = 135°$) in Table 9. The experimental data is presented in the top row of Tables 8 and 9, while the predicted ply-by-ply damage maps are shown below the experimental data starting from the surface ply down to the central ply. The plies are numbered from $i = 1$ for the central ply to $i = 4$ in Laminate 1 and $i = 8$ in Laminate 2 for the surface ply, respectively. In the damage maps, the predicted intra-laminar damage (blue for fibre failure (d_1), red for matrix failure (d_2)) of the i_{th} ply is superimposed on the inter-laminar damage (black for delamination or cohesive surface damage (CSDMG)) in the interface beneath, *i.e.* between ply i and ply (i-1). The approach enables the validation of the FEM meso-scale model predictions against the experiments, and provides additional insight into the critical failure mechanisms, which are discussed in more detail in Section 5.

Note from Table 7, that the ultimate failure load for Laminate 1 loaded in tension-shear ($\alpha = 45°$) is predicted by the model within 1% of the experimental result. The fidelity of the prediction is further supported by the good agreement between the experimentally observed and simulated damage patterns, as shown in Table 8; the high maximum principal strain (ϵ_{max}) concentrations at the hole and at the top right and bottom left corners of the specimens (Table 8,

top row), at both the failure initiation and ultimate load orientated parallel to the fibres of the surface ply, are a clear indication of surface matrix cracks. These surface cracks are also predicted by the model in the surface ply 4 (labelled in Table 8) and match the extent and location of the ϵ_{max} concentrations in the experiment well. Examining the failed specimen in Table 8 at post-P_{ult}, it is observed that the macroscopic crack plane runs diagonally from the bottom left, through the hole, to the top right corner. This is also predicted by the model, where cracks in the surface ply 4 originate at the hole and the bottom left and top right corners as well. Furthermore, two distinct delamination planes (labelled in Table 8, top row at post-P_{ult}) are observed by visual inspection of the failed specimen. In the model predictions they can be associated with delamination at the +45°/90° and -45°/0° interfaces, as labelled in Table 8 at post-P_{ult}. By investigating the model predictions, it can be concluded that fibre kinking at the hole in the −45° ply 3, as labelled in Table 8 at P_{ult} and post-P_{ult}, in combination with delamination at the −45°/0° interface are governing the ultimate strength of Laminate 1 loaded in combined tension-shear. The predicted failure behaviour agrees well with observations in [48] where X-ray Computed Tomography (CT) was used to investigate failure of multidirectional laminates in the combined tension-shear loading regime.

For Laminate 1 loaded in combined compression-shear ($\alpha = 135°$), the model over-predicts failure by 27% in comparison to the experimental data (see Table 7). Nevertheless, some of the governing damage mechanisms are captured as shown in Table 9; at P_{ult}, surface matrix cracks are identified experimentally in the DIC ϵ_{max} maps (labelled in Table 9). These surface cracks in ply 4 are also predicted by the model. Furthermore, prior to the occurrence of visual damage on the surface, the model predicts delamination initiation at the curved edges and at the hole in the −45°/0° interface, and the onset of compressive fibre failure in the −45° ply at the hole. The predicted sub-surface damage can be associated with high localised out-of-plane displacement gradients observed in the DIC displacement map (labelled in Table 9 at failure initiation) and as discussed in [23]. The model predictions indicate that the critical failure event in Laminate 1

loaded in compression-shear is governed by fibre kinking in the −45° and 0° plies in combination with delamination at the hole and the curved edges (labelled in table 9).

From the damage maps it is further observed that the matrix crack and delamination patterns are closely linked, as the delaminated areas are in many cases limited by matrix cracks. An example of this behaviour is seen in Table 8 in ply 4 of Laminate 1 at post-P_{ult}, or in Table 9 in ply 3 at P_{ult}. This indicates that the physics of the critical interaction effects between intra- and inter-laminar failure modes can be captured by the CDM framework in combination with the fibre-aligned mesh.

5   Ply thickness and multi-axial loading effects

In this section, the FEM results are used in combination with the experimental data taken from [23], [34] to analyse the effect of ply thickness on the critical failure mechanisms in multidirectional laminates subjected to combined tension/compression and shear loading. Tables 10 to 12 provide an overview of the critical failure mechanisms predicted in Laminates 1 and 2. The critical failure mechanism is identified by comparing the damage patterns at P_{ult} and post-P_{ult} in the critical plies. In this way, the critical failure event that will eventually lead to the ultimate failure of the specimen can be separated from subcritical events. By inspecting the predicted damage maps for the 16-ply Laminate 2 in [34], it was found that the failure modes/mechanisms in the plies of the same fibre orientation within a specimen are very similar. For this reason, it has been deemed sufficient to show only one ply per fibre orientation angle in the 'thin' ply Laminate 2, for comparison to the 'thick' ply Laminate 1.

For the tensile load case ($\alpha = 0°$), the 'thin' ply Laminate 2 specimens are on average 6% stronger than the 'thick' ply Laminate 1 specimens (see Figure 9). Although the ply thickness effect qualitatively agrees with similar studies in the literature [44], [45], it is less pronounced for the investigated material system and specimen configuration. Furthermore, the effect in the tension load case is small in comparison to the combined tension-shear load cases ($\alpha = 15°$,

45°). The similar open-hole specimen tensile strength ($\alpha = 0°$) is related to a similar critical ultimate failure mode, despite the different UD ply thickness [23]; for the specimens to lose their ultimate load carrying capability, the strong 0° plies must fail in tension in both Laminates. As they have the same amount of 0° fibres (see Table 1), and X_T is barely affected by the ply thickness effect (no in-situ property), both Laminates exhibit a similar open-hole specimen tensile strength. The differences in the extent of subcritical damage mechanisms (matrix cracking and delamination) does therefore not significantly affect the open-hole specimen tensile strength in the two Laminates. Table 10 shows critical failure mechanisms predicted by the FEM model for both Laminate 1 and 2 specimens in tension ($\alpha = 0°$). It is observed from Table 10, that the model unambiguously predicts that the critical ultimate failure event in Laminate 2 is associated with fibre tensile failure (blue) in the 0° plies (labelled in Table 10). The prediction of the expected failure mechanism is also reflected in the accurate prediction of the open-hole tensile specimen strength ($E = -6\%$ in Table 7). On the other hand, the model predicts Laminate 1 to fail due to excessive delamination in the $-45°/0°$ interface, while no fibre breaks in the 0° plies are predicted (see Table 10). In the experiment the specimens break into two, indicating that fibres in the 0° plies have failed following extensive delamination and matrix cracking [23], which is not predicted by the model. This is also reflected by the relatively poor prediction of the open-hole tensile specimen strength for Laminate 1 ($E = -25\%$ in Table 7). The difficulty in predicting the failure mechanism in Laminate 1 is associated with the challenge of modelling extensive subcritical damage (delamination, fibre splitting, matrix cracking), while avoiding premature failure prediction due to subcritical damage before the high-energy ultimate failure event (fibre tensile failure). Furthermore, it is also likely that the lack of inter-laminar experimental characterisation contributes to the observed discrepancies in the prediction of subcritical damage development.

While the experimental strength of Laminate 1 and 2 specimens in tension ($\alpha = 0°$) is similar, Laminate 2 specimens are up to 147% stronger in combined tension-shear ($\alpha = 15°$), as shown

in Figure 9. The predicted critical failure mechanisms for both Laminates are similar to the tension load case (compare Tables 10 and 11). Laminate 1 is predicted to be prone to delamination failure at the −45°/0° interface, Laminate 2 is predicted to ultimately fail due to fibre tensile failure in the 0° plies. The predicted ultimate failure strengths for the combined tension-shear load case ($\alpha = 15°$) are both within 10% of the experimental values, hence supporting the fidelity of the predicted failure mechanism. In the case of Laminate 1, ultimate failure is indeed governed by delamination, so the 0° plies do not need to fail for the specimen to lose its maximum load bearing capability (different from the tension load case ($\alpha = 0°$)). Therefore, the critical failure event is now influenced by the in-situ ply thickness effect, resulting in the experimentally observed strength difference in combined tension-shear loading ($\alpha = 15°$) between 'thick' and 'thin' ply laminates.

The critical failure mechanisms for both Laminates in the shear-dominated ($\alpha = 45°$, 90°, 135°) and compression-dominated ($\alpha = 180°$) load cases are similar and dominated by fibre kinking failure in the −45° and 0° plies, as well as delamination, as shown in Table 12. In the combined tension-shear ($\alpha = 45°$) load case (also see Table 8), both laminates show the onset of fibre kinking failure at the hole in the −45° plies (labelled in Table 12) under compressive longitudinal tensile stress induced by the shear load component (N_{xy}). For Laminate 2, this is likely to be the critical failure event, while Laminate 1 also exhibits an extensive delamination at the −45°/0° ply interface. The delamination in Laminate 1 is the critical ultimate failure event and explains the strength difference observed between Laminates 1 and 2 in Figure 9. The critical failure event in both Laminates in the shear load case ($\alpha = 90°$), is fibre kinking failure at the hole in the −45° plies. Compressive fibre stresses are induced in the −45° plies by the shear load component (N_{yx}). The critical failure mode remains fibre kinking for both laminates loaded in combined compression-shear ($\alpha = 135°$), but not only the −45° plies but also the 0° plies exhibit extensive fibre compressive damage (also see Table 9 for Laminate 1). For uniaxial compression ($\alpha = 180°$), the critical failure event changes from fibre kinking in the −45° plies to

fibre kinking in the 0° plies near the hole due to the fibre compressive stresses induced by the compressive load component (N_y). Overall, it is observed that the model predicts Laminate 1 interfaces to be more prone to delamination than Laminate 2 interfaces for all load cases (compare the extent of black delaminated areas in Tables 10 to 12), which is in agreement with related experimental studies on the effect of ply thickness on delamination [2,44,45]. The similar open-hole specimen strength for shear ($\alpha = 90°$), combined compression-shear ($\alpha = 135°$) and compression ($\alpha = 180°$), as observed in Figure 9, can be related to the same critical failure mechanism, *i.e.* fibre kinking in the −45° and 0° plies.

6   Conclusions

A meso-scale FEM modelling framework based on [4,26,27] has been developed and used to simulate failure in quasi-isotropic carbon/epoxy composite open-hole specimens subjected to combined tension/compression and shear loading. The predictive capability of the model was assessed/validated against experimental data previously obtained using a modified Arcan fixture (MAF) combined with stereo digital image correlation (DIC) [23]. The main findings of the model assessment are:

1. The multi-axial open-hole specimen strength for the two laminates with different ply thicknesses was predicted with a mean relative error of 15% across all of the investigated load cases, and a maximum relative error of 27% in the combined compression-shear load case. This is an encouraging result, given that similar modelling frameworks predict uniaxial open-hole tension and compression strengths for well-characterised material systems within 10% of the experimental results [4,6,7,10,14,17,20,21].

2. It has been shown that the adopted continuum damage model (CDM) cannot accurately predict fibre splitting and fibre breaks in regions of high fibre tensile and shear stresses for the investigated material system. This results in an underprediction of the failure strengths

in tensile-dominated load cases. It has been shown that limiting the maximum allowable shear damage alleviates the model limitation and better strength predictions can be obtained.

3. When limiting the maximum allowable shear damage, the open-hole tensile strengths of 'thick' and 'thin' ply laminate specimens were found to be of similar magnitude and in agreement with the experimental results. This is because the critical 0° fibre tensile failure event is not significantly affected by the thickness of the ply.

4. For combined tension-shear loading, the model correctly predicted that the 'thin' ply specimens are stronger than the 'thick' ply specimens. This was attributed to an increased resistance of the 'thin' ply laminate to matrix cracking and delamination observed in the predicted ply-by-ply damage patterns, demonstrating the ability of the model to capture ply constraining (or in-situ) effects.

5. For shear, combined compression-shear, and compression loading, the model predicted similar critical failure events *i.e.* fibre kinking in the −45° and 0° plies. The predicted ply thickness effect diminishes with increased compression, which is in agreement with the experimental results.

6. Future work to overcome the model limitation in tensile-dominated load cases should include the introduction of a finite strain formulation in the CDM framework.

This work has clearly demonstrated the need for continuous and rigorous model assessment and validation against high-fidelity experimental data for new material systems and complex loading conditions. Multi-axial coupon tests, such as with the MAF, have been showcased as useful tools to scrutinise and challenge modelling frameworks to enable further progression towards reliable 'virtual testing'.

Acknowledgements

References

[1]   Tan JLY, Deshpande VS, Fleck NA. The effect of laminate lay-up on the multi-axial notched strength of CFRP panels: Simulation versus experiment. Eur J Mech A/Solids 2017;66:309–21. https://doi.org/10.1016/j.euromechsol.2017.08.002.

[2]   Guillamet G, Turon A, Costa J, Renart J, Linde P, Mayugo JA. Damage occurrence at edges of non-crimp-fabric thin-ply laminates under off-axis uniaxial loading. Compos Sci Technol 2014;98:44–50. https://doi.org/10.1016/j.compscitech.2014.04.014.

[3]   Davies G, Ankersen J, Guiamatsia I, Gordon B. Replacement of industrial testing composite structures by simulation. J Aerosp Eng 2010;224:471. https://doi.org/10.1243/09544100JAERO570.

[4]   Furtado C, Catalanotti G, Arteiro A, Gray PJ, Wardle BL, Camanho PP. Simulation of failure in laminated polymer composites: Building-block validation. Compos Stuctures 2019;226.

[5]   Maimí P, Camanho PP, Mayugo JA, Davila CG. A continuum damage model for composite laminates: Part I - Constitutive model. Mech Mater 2007;39:897–908. https://doi.org/10.1016/j.mechmat.2007.03.005.

[6]   Maimí P, Camanho PP, Mayugo JA, Dávila CG. A continuum damage model for composite laminates: Part II - Computational implementation and validation. Mech Mater 2007;39:909–19. https://doi.org/10.1016/j.mechmat.2007.03.006.

[7]   Falcó O, Ávila RL, Tijs B, Lopes CS. Modelling and simulation methodology for unidirectional composite laminates in a Virtual Test Lab framework. Compos Struct

2018;190:137–59. https://doi.org/10.1016/j.compstruct.2018.02.016.

[8] Zhuang F, Chen P, Arteiro A, Camanho PP. Mesoscale modelling of damage in half-hole pin bearing composite laminate specimens. Compos Struct 2019;214:191–213. https://doi.org/10.1016/j.compstruct.2019.01.062.

[9] Tan JLY, Deshpande VS, Fleck NA. Prediction of failure in notched polymer laminates under multi-axial loading. Philos Trans A 2016;374.

[10] Abisset E, Daghia F, Ladevze P. On the validation of a damage mesomodel for laminated composites by means of open-hole tensile tests on quasi-isotropic laminates. Compos Part A Appl Sci Manuf 2011;42:1515–24. https://doi.org/10.1016/j.compositesa.2011.07.004.

[11] Hallett SR, Green BG, Jiang WG, Wisnom MR. An experimental and numerical investigation into the damage mechanisms in notched composites. Compos Part A Appl Sci Manuf 2009;40:613–24. https://doi.org/10.1016/j.compositesa.2009.02.021.

[12] Bouvet C, Castanié B, Bizeul M, Barrau JJ. Low velocity impact modelling in laminate composite panels with discrete interface elements. Int J Solids Struct 2009;46:2809–21. https://doi.org/10.1016/j.ijsolstr.2009.03.010.

[13] Serra J, Bouvet C, Castanié B, Petiot C. Experimental and numerical analysis of Carbon Fiber Reinforced Polymer notched coupons under tensile loading. Compos Struct 2017;181:145–57. https://doi.org/10.1016/j.compstruct.2017.08.090.

[14] Archard V, Bouvet C, Castanié B, Chirol C. Discrete ply modelling of open hole tensile tests. Compos Stuctures 2019;113:369–81. https://doi.org/.1037//0033-2909.I26.1.78.

[15] Moes N, Dolbow J, Belytschko T. A finite element method for crack growth without remeshing. Int J Numer Methods Eng 1999;46:131–50.

[16] Iarve E V, Gurvich MR, Mollenhauer DH, Rose CA, Dávila CG. Mesh-independent matrix cracking and delamination modeling in laminated composites. Int J Numer Meth Engng 2011;88:749–73. https://doi.org/10.1002/nme.

[17] Iarve E V., Hoos K, Braginsky M, Zhou E, Mollenhauer DH. Progressive failure

simulation in laminated composites under fatigue loading by using discrete damage modeling. J Compos Mater 2017;51:2143–61. https://doi.org/10.1177/0021998316681831.

[18]   Bažant ZP, Oh BH. Crack band theory for fracture of concrete. Mater Struct 1983;16:155–77.

[19]   Maimí P, Camanho PP, Mayugo JA, Dávila CG. A Thermodynamically Consistent Damage Model for Advanced Composites. NASA/TM-2006-214282. Nasa Tm 2006:47.

[20]   Hallett SR, Green BG, Kin WJ, Cheung H, Wisnom MR. The open hole tensile test : a challenge for virtual testing of composites. Int J Fract 2009;158:169–81. https://doi.org/10.1007/s10704-009-9333-8.

[21]   Hallett SR, Green BG, Jiang WG, Wisnom MR. An experimental and numerical investigation into the damage mechanisms in notched composites. Compos Part A Appl Sci Manuf 2009;40:613–24. https://doi.org/10.1016/j.compositesa.2009.02.021.

[22]   Kureemun U, Ridha M, Tay T. Biaxial tensile-compressive loading of unnotched and open-hole carbon epoxy crossply laminates. J Compos Mater 2014;49:2817–37. https://doi.org/10.1177/0021998314555043.

[23]   Laux T, Gan KW, Dulieu-Barton JM, Thomsen OT. Ply thickness and fibre orientation effects in multidirectional composite laminates subjected to combined tension/compression and shear. Compos Part A Appl Sci Manuf 2020;133. https://doi.org/10.1016/j.compositesa.2020.105864.

[24]   Gan KW, Laux T, Taher ST, Dulieu-Barton JM, Thomsen OT. A novel fixture for determining the tension/compression-shear failure envelope of multidirectional composite laminates. Compos Struct 2018;184:662–73. https://doi.org/10.1016/j.compstruct.2017.10.030.

[25]   Laux T, Gan KW, Dulieu-Barton JM, Thomsen OT. A simple nonlinear constitutive model based on non-associative plasticity for UD composites: Development and calibration using a Modified Arcan Fixture. Int J Solids Struct 2019;162:135–47.

https://doi.org/10.1016/j.ijsolstr.2018.12.004.

[26] Camanho PP, Davila CG, Moura D. Numerical Simulation of Mixed-Mode Progressive Delamination in Composite Materials Damage and Failure of Non-Conventional Composite Laminates View project. J Compos Mater 2003;37:1415–38. https://doi.org/10.1177/002199803034505.

[27] Turon A, Camanho PP, Costa J, Dávila CG. A damage model for the simulation of delamination in advanced composites under variable-mode loading. Mech Mater 2006;38:1072–89. https://doi.org/10.1016/j.mechmat.2005.10.003.

[28] Dávila CG, Camanho PP, Rose CA. Failure criteria for FRP laminates. J Compos Mater 2005;39:323–45. https://doi.org/10.1177/0021998305046452.

[29] Pinho ST, Dávila CG, Camanho PP, Iannucci L, Robinson P. Failure models and criteria for FRP under in-plane or three-dimensional stress states including shear non-linearity. 2005. https://doi.org/NASA/TM-2005-213530.

[30] Hinton MJ, Soden PD. Predicting failure in composite laminates: the background to the exercise. Compos Sci Technol 1998;58:1001–10. https://doi.org/10.1016/S0266-3538(98)00074-8.

[31] Hinton MJ, Kaddour AS. The background to the second world-wide failure exercise. J Compos Mater 2012;46:2283–94. https://doi.org/10.1177/0021998312449885.

[32] Kaddour A, Hinton M, Smith P. The background to the third world-wide failure exercise. J Compos Mater 2013;47:2417–26. https://doi.org/10.1177/0021998313499475.

[33] Daniel IM, Ishai O. Engineering mechanics of composite materials. Oxford University Press; 2005.

[34] T. Laux. Experimental and computational characterisation of composite laminates subjected to multiaxial loading. PhD thesis. University of Southampton, 2020.

[35] Dassault System. Abaqus 6.14 Documentation 2017.

[36] Robert McNeel & Associates. Rhinoceros 3D 2020.

[37] Furtado C. Damage and fracture in advanced composite laminates: thin- ply and

nanoengineered composites. PhD thesis. Univerity of Porto, 2020.

[38]   Camanho PP, Arteiro A, Melro AR, Catalanotti G, Vogler M. Three-dimensional invariant-based failure criteria for fibre-reinforced composites. Int J Solids Struct 2015;55:92–107. https://doi.org/10.1016/j.ijsolstr.2014.03.038.

[39]   Parvizi A, Garrett KW, Bailey JE. Constrained cracking in glass fibre-reinforced epoxy cross-ply laminates. J Mater Sci 1978;13:2131–6. https://doi.org/10.1007/BF00541666.

[40]   Chang F, Chen M. The in situ ply shear strength distributions in graphite/epoxy laminated composites. J Compos Mater 1986;21:708–33.

[41]   Arteiro A, Catalanotti G, Melro AR, Linde P, Camanho PP. Micro-mechanical analysis of the effect of ply thickness on the transverse compressive strength of polymer composites. Compos Part A Appl Sci Manuf 2015;79:127–37. https://doi.org/10.1016/j.compositesa.2015.09.015.

[42]   Camanho PP, Davila CG, Pinho ST, Iannucci L, Robinson P. Prediction of in situ strengths and matrix cracking in composites under transverse tension and in-plane shear. Compos Part A Appl Sci Manuf 2006;37:165–76. https://doi.org/10.1016/j.compositesa.2005.04.023.

[43]   BS EN ISO 14130: Fibre-reinforced plastic composites Determination of apparent interlaminar shear strength by short-beam method 1998.

[44]   Green BG, Wisnom MR, Hallett SR. An experimental investigation into the tensile strength scaling of notched composites. Compos Part A Appl Sci Manuf 2007;38:867–78. https://doi.org/10.1016/j.compositesa.2006.07.008.

[45]   Wisnom MR, Hallett SR. The role of delamination in strength, failure mechanism and hole size effect in open hole tensile tests on quasi-isotropic laminates. Compos Part A Appl Sci Manuf 2009;40:335–42. https://doi.org/10.1016/j.compositesa.2008.12.013.

[46]   Tijs BHA., A T, Chiara B. The importance of accounting for large shear deformations on modelling matrix failure of hermoplastic and thermoset composites. 7th Themat. Conf. Mech. Response Compos., Girona, Spain: 2019.

Laux T., Gan K. W., Tavares R.P., Furtado C., Arteiro A., Camanho P.P., Thomsen O.T., Dulieu-Barton J.M., Modelling damage in multidirectional laminates subjected to multi-axial loading: ply thickness effects and model assessment, Composite structures (2021), doi: https://doi.org/10.1016/j.compstruct.2021.113766

[47] Eskandari S, Andrade Pires FM, Camanho PP, Marques AT. Intralaminar damage in polymer composites in the presence of finite fiber rotation: Part I – Constitutive model. Compos Struct 2016;151:114–26. https://doi.org/10.1016/j.compstruct.2016.01.047.

[48] Tan JLY, Deshpande VS, Fleck NA. Failure mechanisms of a notched CFRP laminate under multi-axial loading. Compos Part A Appl Sci Manuf 2015;77:56–66. https://doi.org/10.1016/j.compositesa.2015.06.005.

[49] BS EN ISO 527-5:2009: Plastics — Determination of tensile properties, Part 5: Test conditions for unidirectional fibre-reinforced plastic composites 1996.

[50] ASTM D3410/D3410M-03, Standard test method for compressive properties of polymer matrix composite mterials with unsupported gage section by shear 2003. https://doi.org/10.1520/D3410.
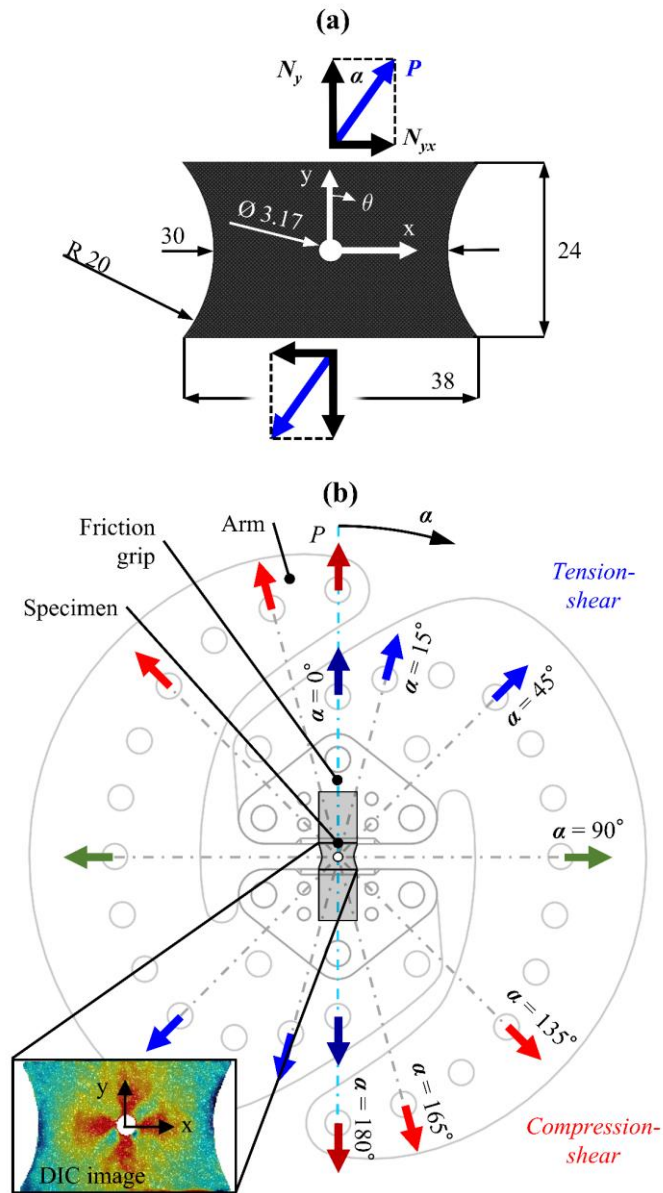
Figure 1. The modified Arcan fixture (MAF) experiment: (a) the modified open-hole specimen, and (b) the MAF with the specimen installed.
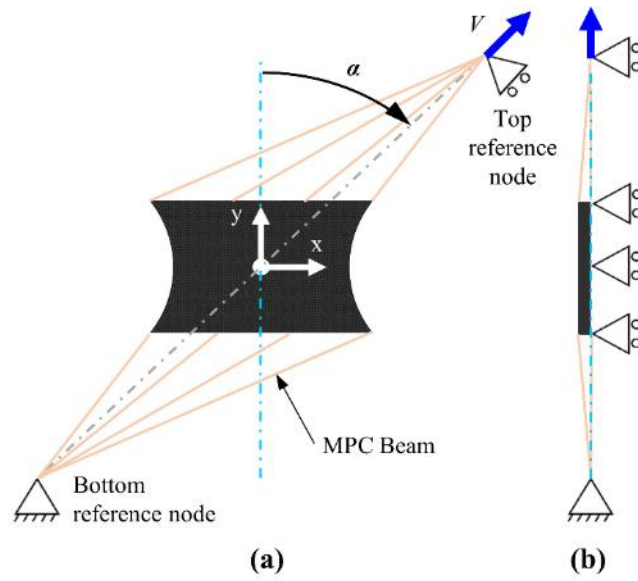
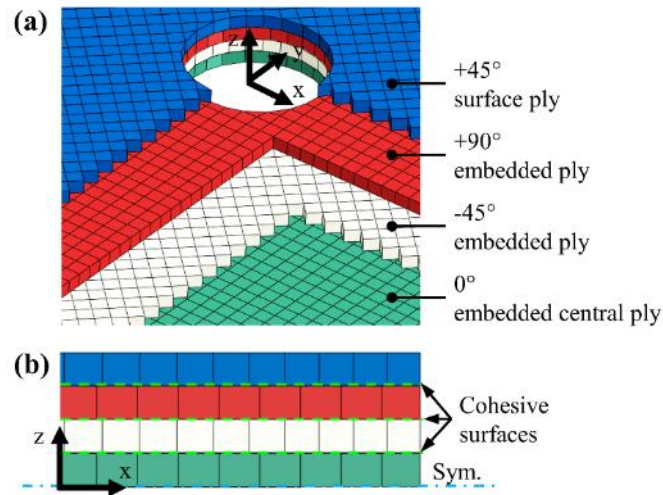Figure 2. Mimicking the MAF boundary conditions in model space: (a) plane view, (b) side view.

Figure 3. Meso-scale modelling framework illustrated on the Laminate 1 model: (a) 3D solid elements for UD plies with structured, fibre-aligned mesh, and (b) cross section showing cohesive surfaces in between the solid UD plies.
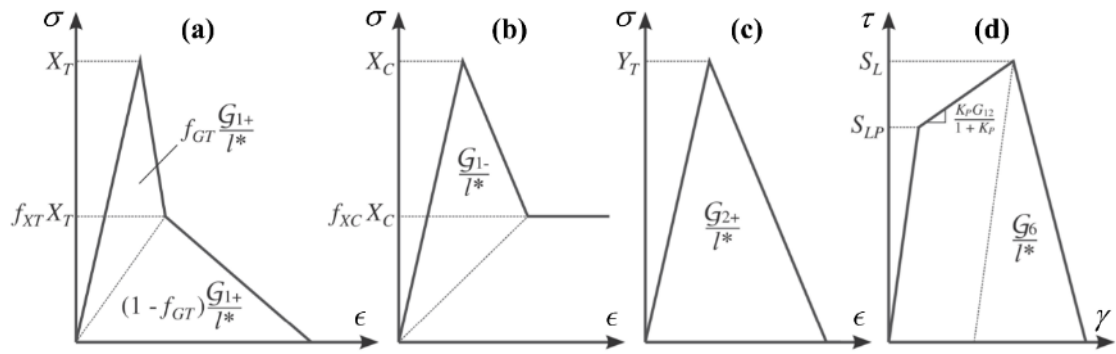
Figure 4. The uniaxial stress-strain responses in (a) longitudinal tension, (b) longitudinal compression, (c) transverse tension and compression and (d) in-plane shear [4].
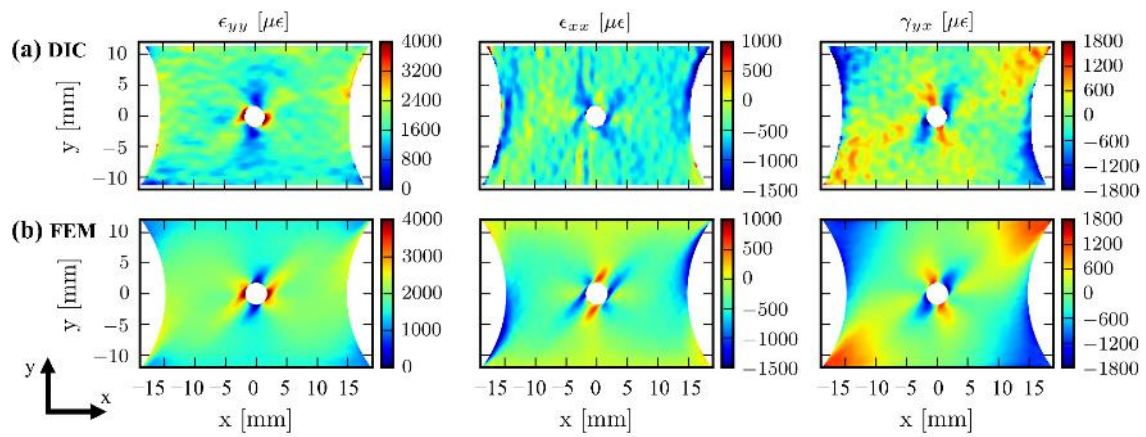
Figure 5. Surface strain fields in Laminate 1 specimen subjected to uniaxial tension ($\alpha = 0°$) at $P = 7.5$ kN; (a) DIC measurements and (b) FEM predictions.
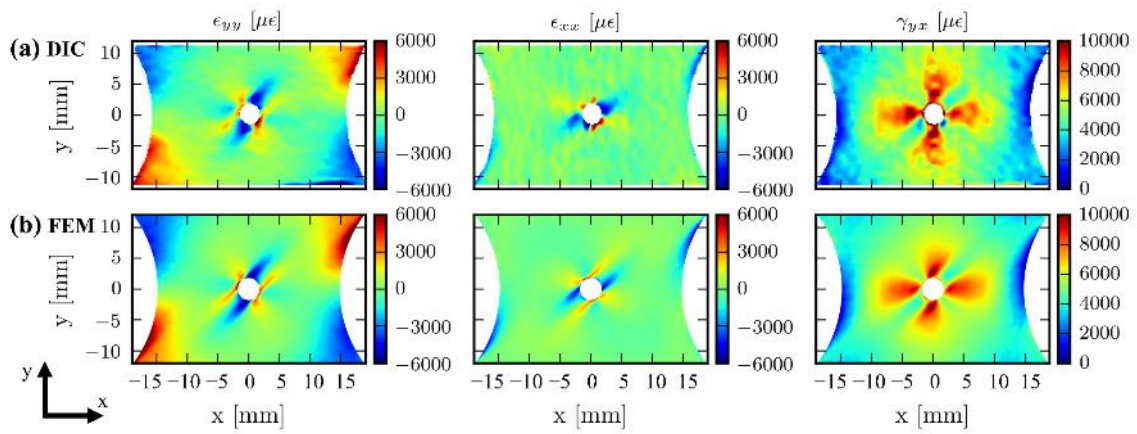
Figure 6. Surface strain fields in Laminate 1 specimen subjected to uniaxial shear ($\alpha = 90°$) at $P = 7.5$ kN; (a) DIC measurements and (b) FEM predictions.
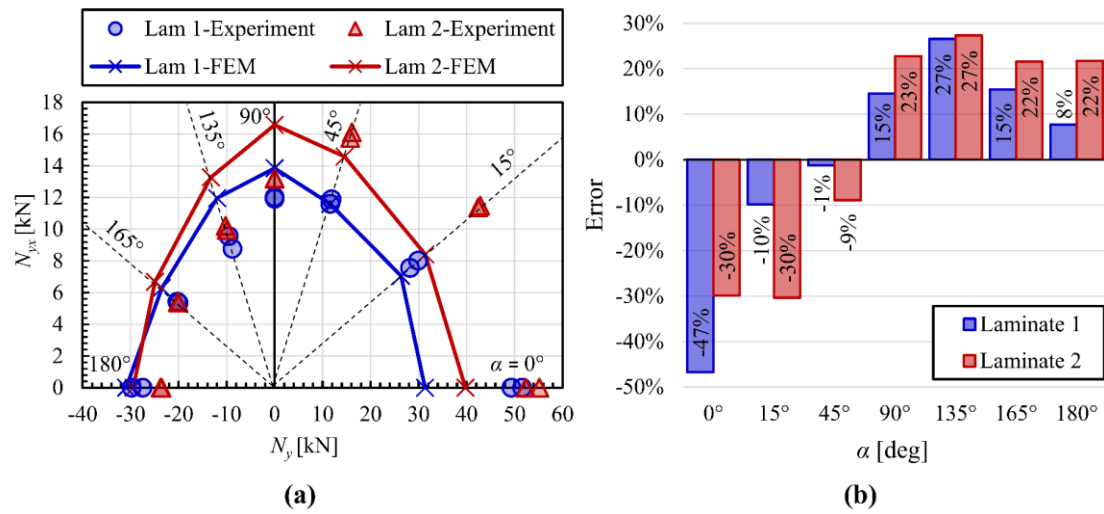
Figure 7. Experimental results from [23] vs. initial model predictions: (a) tension/compression-shear failure envelopes, and (b) difference between model prediction and experimental ultimate specimen strength results.
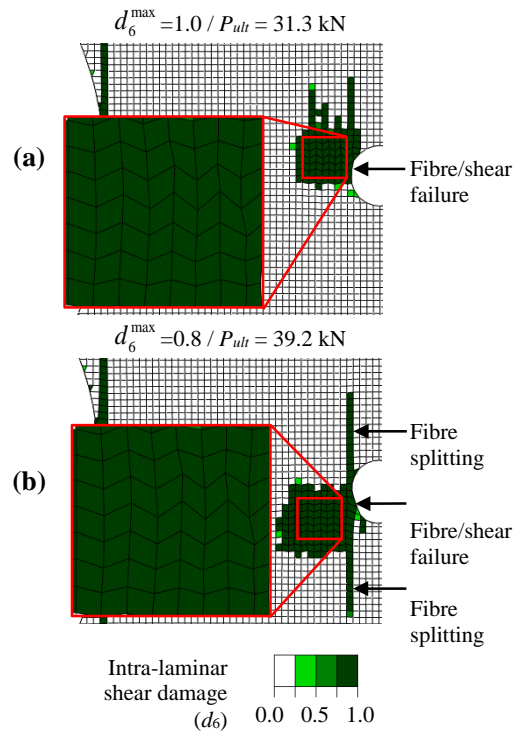
Figure 8. Predicted failure mechanisms of the 0° ply in Laminate 1 under tension ($\alpha = 0°$) just after peak load: (a) $d_6^{max} = 1.0$ and (b) $d_6^{max} = 0.8$.
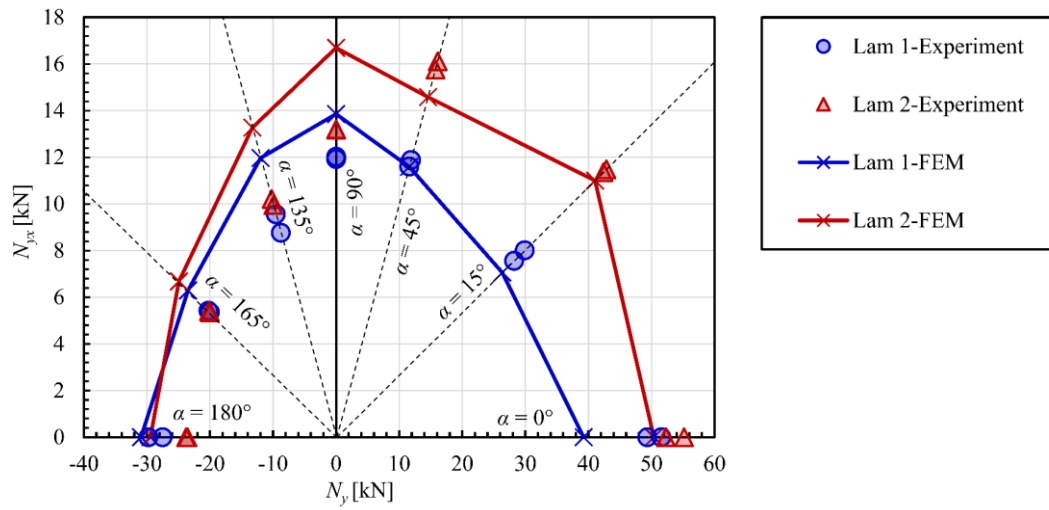
Figure 9. Combined tension/compression-shear open-hole specimen failure envelopes: experimental data from [23] vs. improved FEM model predictions.

Table 1. Quasi-isotropic carbon epoxy laminates tested.

Designation	'thick' ply Laminate 1	'thin' ply Laminate 2
Lay-up	$[45/90/-45/0]_s$	$[(45*/90/-45/0)_2]_s$
t_{lam} [mm] (% CoV)	2.326 (1.29%)	2.133 (2.71%)
t_{ply} [mm]	0.29100	0.14550

* Half thickness ply t_{ply} = 0.07275 mm

Table 2. Elastic properties of the UD ply [34].

E_1 [MPa] (% CoV)	143190 (1.83)	ISO 527-5 [49]
E_{1c} [MPa] (% CoV)	142620 (3.45)	ASTM D3410 [50]
E_2 [MPa] (% CoV)	7900 (0.12)	ISO 527-5 [49]
G_{12} [MPa] (% CoV)	3940 (0.33)	MAF test [34]
v_{12} (% CoV)	0.328 (5.6)	ISO 527-5 [49]

Table 3. Strengths of the UD ply [34].

X_T [MPa] (% CoV)	2774 (1.05)	ISO 527-5 [49]
X_C [MPa] (% CoV)	1394 (2.21)	ASTM D3410 [50]
Y_T [MPa] (% CoV)	52 (8.70)	ISO 527-5 [49]
Y_C [MPa] (% CoV)	173 (0.75)	ASTM D3410 [50]
S_L [MPs] (% CoV)	81 (4.86)	BS EN ISO 14130 [43]
S_L^P [MPa]	60	MAF test [34]
K_P [MPa]	0.076	
Y_{BT} [MPa]	32	Scaled as in [4]
Y_{BC} [MPs]	410	Scaled as in [4]

Table 4. UD ply fracture toughness values and softening law shape parameters [4].

$\mathscr{G}_{2+}$ [kJ/m2]	0.28	IM7/8775 [4]
$\mathscr{G}_{2-}$ [kJ/m2]	1.31	IM7/8775 [4]
$\mathscr{G}_{6}$ [kJ/m2]	0.79	IM7/8775 [4]
$\mathscr{G}_{1+}$ [kJ/m2]	340	T800/M21 [4]
f_{XT}	0.4	T800/M21 [4]
f_{GT}	0.52	T800/M21 [4]
$\mathscr{G}_{1-}$ [kJ/m2]	61	IM7/8775 [4]
f_{XC}	0.2	IM7/8775 [4]

Table 5. Calculated in-situ strengths based on the UD material properties.

	Laminate 1	Laminate 2
Embedded central ply		
t_{ply} [mm]	0.5820	0.2910
Y_T^{is} [MPa]	82.36	98.67
S_L^{is} [MPa]	99.19	99.19
Y_C^{is} [MPa]	211.35	211.35
Embedded ply		
t_{ply} [mm]	0.2910	0.1455
Y_T^{is} [MPa]	98.67	139.54
S_L^{is} [MPa]	99.19	99.19
Y_C^{is} [MPa]	211.35	211.35
Surface ply		
t_{ply} [mm]	0.2910	0.07275
Y_T^{is} [MPa]	62.10	124.19
S_L^{is} [MPa]	81.19	84.81
Y_C^{is} [MPa]	173.00	180.72

Table 6. Interface (cohesive zone) material parameters.

K_n [MPa]	10^6	[26]
τ_n [MPa]	52	Equal to Y_T
τ_{sh} [MPa]	81.19	ISO 14130 [43]
G_{IC} [kJ/m2]	0.28	IM7/8552 [4]
G_{IIC} [kJ/m2]	0.79	IM7/8552 [4]
η_{B-K}	1.45	IM7/8552 [4]

Table 7. Multi-axial open-hole strength: final relative errors (E) for each simulation and mean relative errors.

Load case (α)	Error E (%)		
	Laminate 1	**Laminate 2**	**Mean**
0° tension	−25*	−6*	**16**
15°	−10	−4**	**7**
45°	−1	−9	**5**
90° shear	15	23	**19**
135°	27	27	**27**
165°	15	22	**18**
180° compression	8	22	**15**
Mean all load cases	**14**	**16**	15
Mean tension-shear	**13**	**11**	12
Mean compression-shear	**16**	**23**	20

* $d_6^{\max} = 0.8$ in 0° plies

** $d_6^{\max} = 0.8$ in 0° and +45° plies

Table 8. Predicted ply-by-ply damage maps compared to experimental data for Laminate 1 subjected to combined tension-shear loading ($\alpha = 45°$).
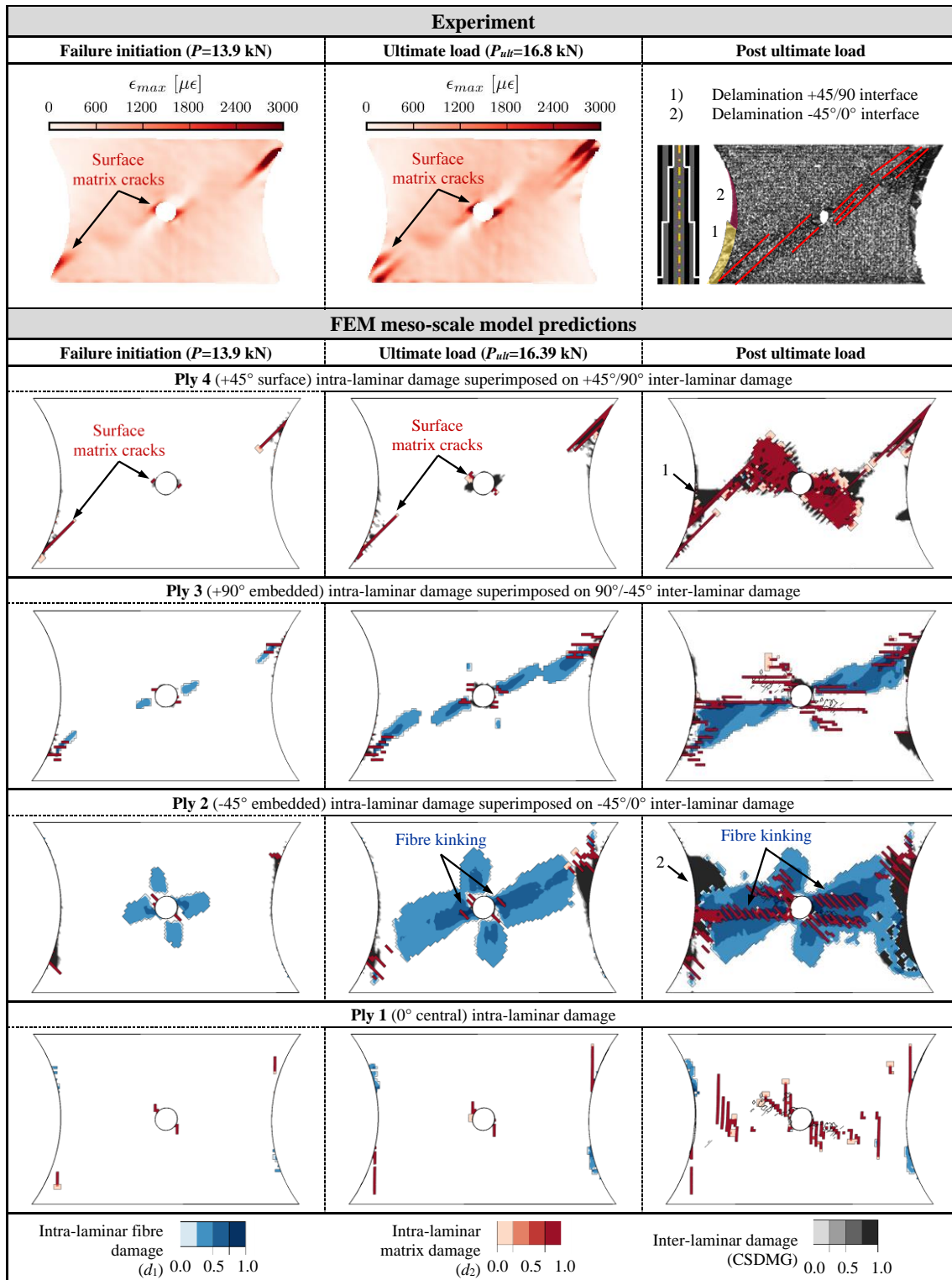

44

Table 9. Predicted ply-by-ply damage maps compared to experimental data for Laminate 1 subjected to combined compression-shear loading ($\alpha = 135°$).
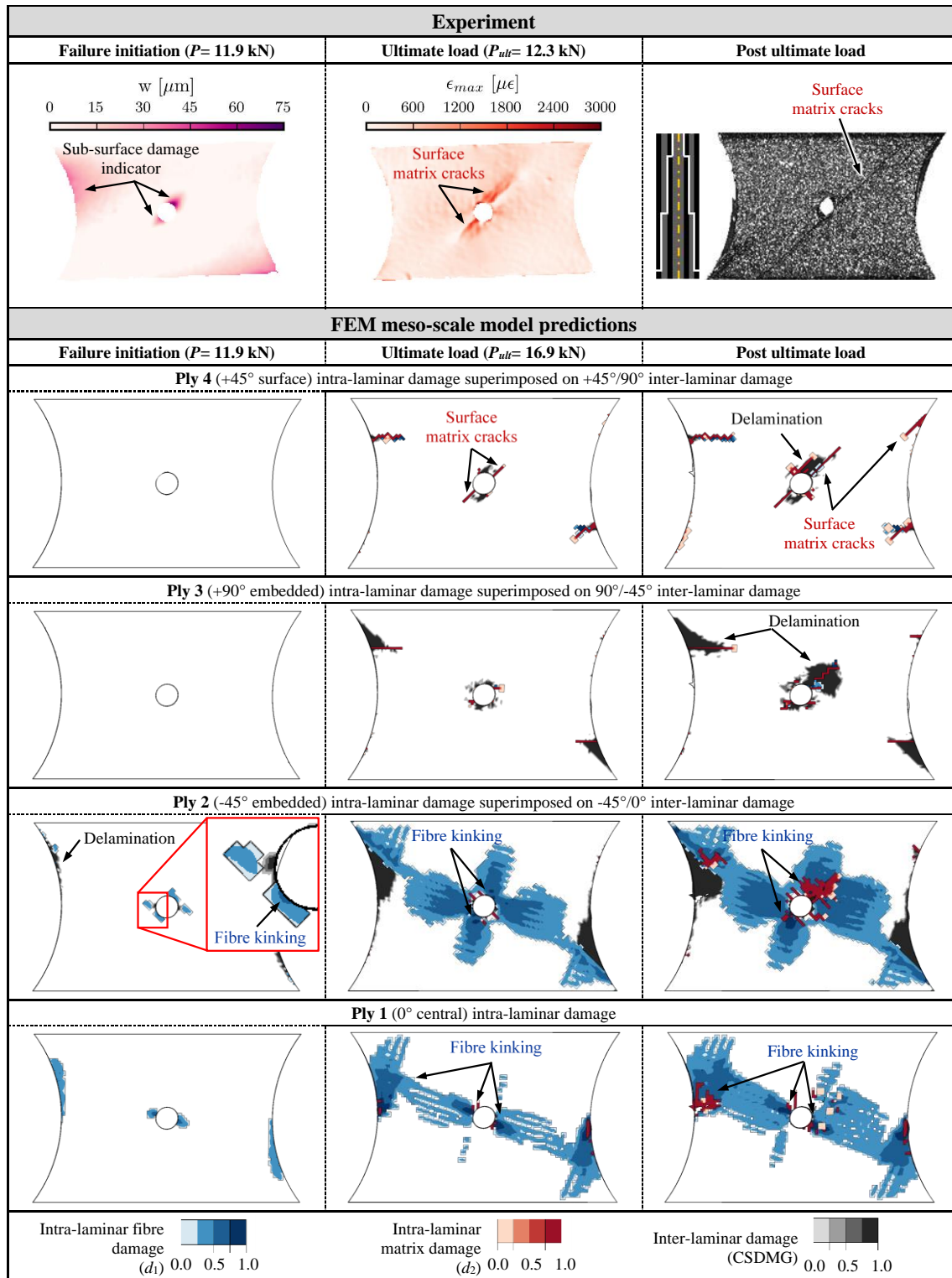
Table 10. Predicted critical ultimate failure events in Laminate 1 and 2 specimens subjected to uniaxial tension ($\alpha = 0°$): damage patterns at ultimate failure load (P_{ult}) and post ultimate failure (post-P_{ult}).
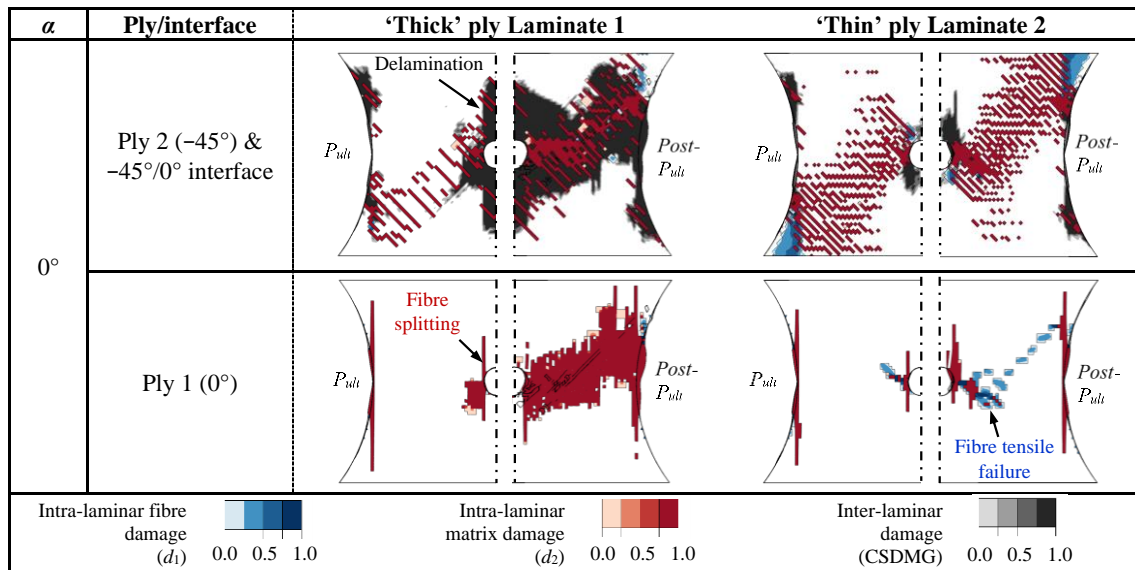
Table 11. Predicted critical ultimate failure events in Laminate 1 and 2 specimens subjected to combined tension-shear ($\alpha = 15°$): damage patterns at ultimate failure load (P_{ult}) and post ultimate failure (post-P_{ult}).
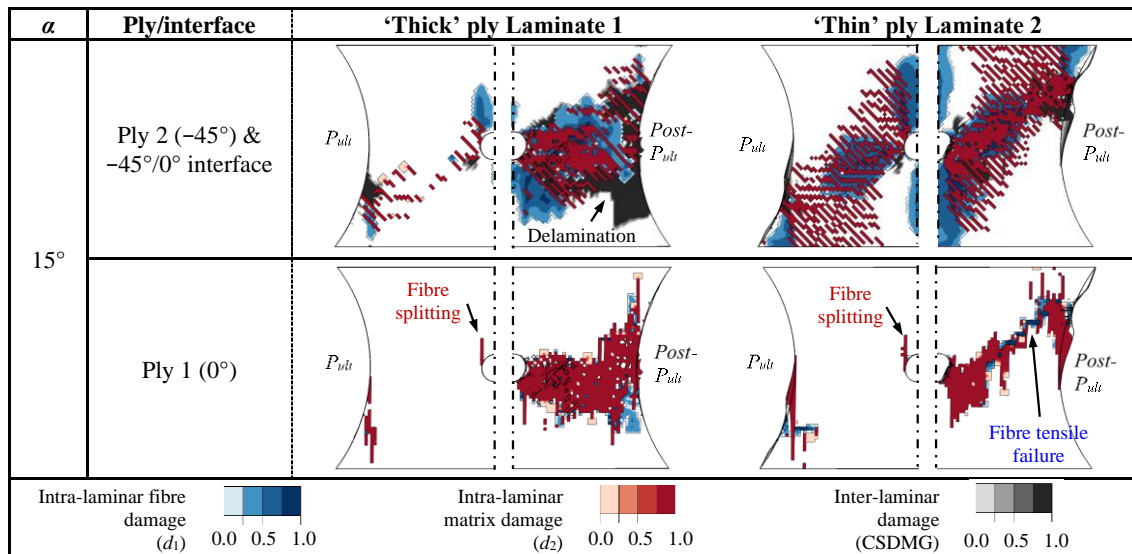
Table 12. Critical failure mechanisms in Laminate 1 (left) and Laminate 2 (right) specimens subjected to combined tension-shear ($\alpha = 45°$), shear ($\alpha = 90°$), combined compression-shear ($\alpha = 135°$), and compression ($\alpha = 180°$): damage patterns at ultimate load (P_{ult}) and post ultimate failure (post-P_{ult}).